Surface deformation and source modeling of Ayaz-Akhtarma mud volcano, Azerbaijan, as detected by ALOS/ALOS-2 InSAR

Kento Iio[1,3*] and Masato Furuya[2]

Abstract

Azerbaijan, located on the western edge of the Caspian Sea in Central Asia, has one of the highest populations of mud volcanoes in the world. We used satellite-based synthetic aperture radar (SAR) images derived from two L-band SAR satellites, ALOS/PALSAR along an ascending track from 2006 to 2011, and its successor ALOS-2/PALSAR-2 along both ascending and descending tracks from 2014 to 2017. First, we applied interferometric SAR (InSAR) technique to detect surface displacements at the Ayaz-Akhtarma mud volcano in Azerbaijan. The 35 derived interferograms indicate that the deformation of the mud volcano is largely characterized by horizontal displacement. Besides the InSAR technique, we also used multiple-aperture interferometry (MAI) to derive the surface displacements parallel to the satellite flight direction to complement the InSAR data. Using the InSAR and MAI data, we obtained 3D displacements, which indicate that the horizontal displacement is dominant relative to subsidence and possible uplift. To explain the displacements, we performed source modeling, based on the assumption of elastic dislocation theory in a half space. The derived model consists of a convex surface on which normal-fault-type slips are semi-radially distributed, causing the significant horizontal displacements with minor subsidence. The convex source surface suggests that a steady overpressure system would be maintained by constantly intruding mud and gas.

Keywords: Mud volcano, Surface deformation, Geodesy, Interferometric synthetic aperture radar, Multiple-aperture interferometry, Advanced Land Observing Satellite, Elastic dislocation model

Introduction

Mud volcanism is analogous to magmatic volcanism; however, the materials extruded to the surface are mud, gases (mostly methane), and saline water originating from deeper sediments. While mud volcanoes include a variety of surface features generated from the extruded materials, their morphology is basically a cone-shaped topographic high, though some can be relatively flat and can even include depressions or calderas. The size of mud volcanoes is generally smaller than that of magmatic volcanoes, but varies over a wide range, from tens of centimeters to several hundred meters in height and tens of kilometers in diameter (Kopf 2002; Dimitrov,

2002; Mazzini and Etiope 2017). Mud volcanoes are distributed both onshore and offshore, but are usually found in active tectonic settings, such as fold-and-thrust belts, accretionary complexes, and convergent plate margins (e.g., Milkov 2000; Kopf 2002; Dimitrov, 2002; Mazzini 2009; Bonini 2012; Mazzini and Etiope 2017), where we may expect compressive stress regimes and higher sedimentation rates. Also, the presence of mud volcanoes is often associated with petroleum systems (Dimitrov, 2002; Kopf, 2002; Mazzini and Etiope 2017). Multiple mechanisms are necessary to account for the formation of mud volcanoes. The first is the bulk density contrast between lighter clays and denser overburden in sedimentary layers, which will lead to the formation of mud diapirs. However, the buoyancy of mud diapirs is not strong enough alone for the formation of mud volcanoes, and additional overpressure is regarded as another requirement in their formation. The overpressure is

* Correspondence: knt-iio25@frontier.hokudai.ac.jp
[1]Department of Natural History Sciences, Graduate School of Science, Hokkaido University, N10W8, Kita-ku, Sapporo 060-0810, Japan
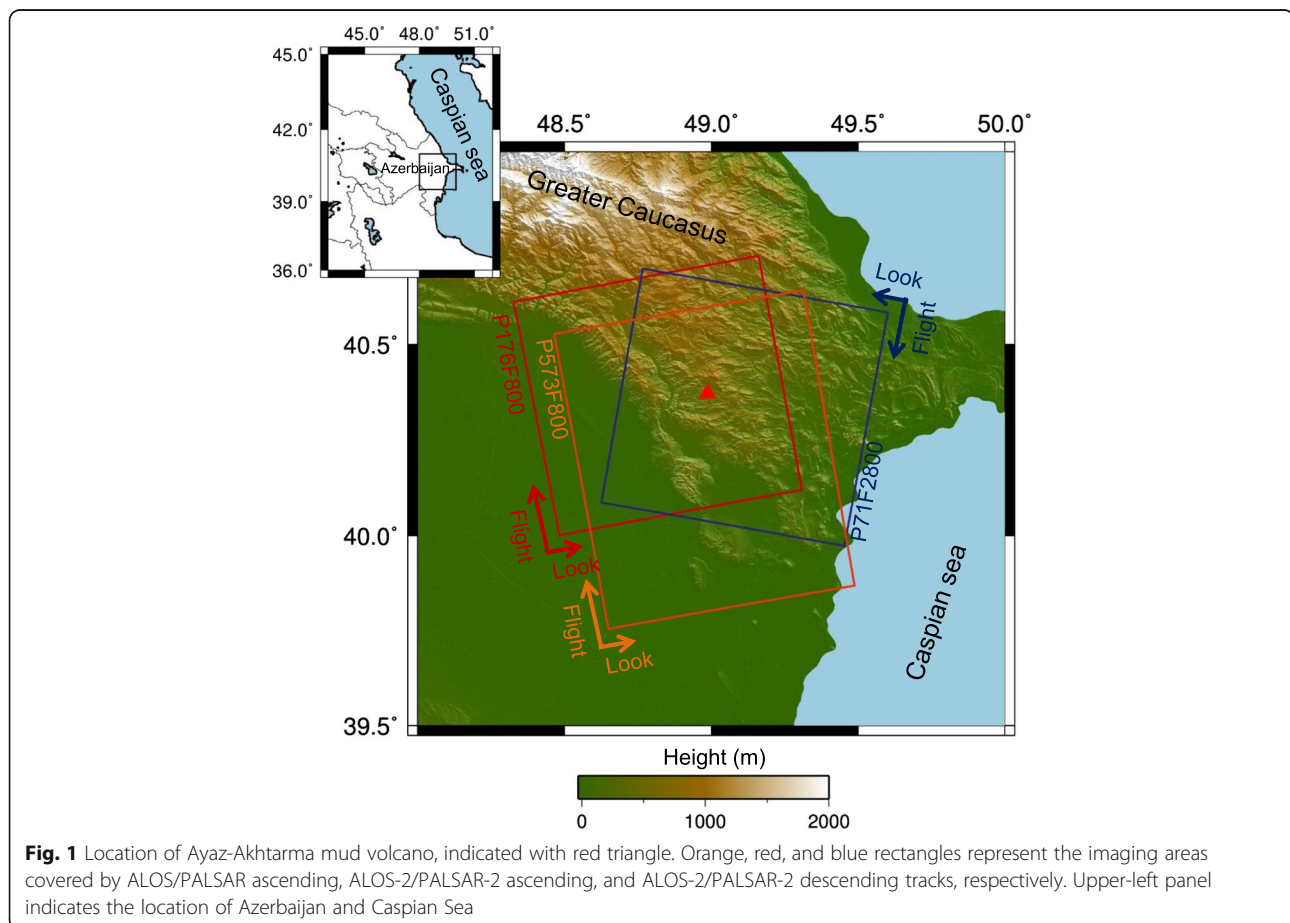[3]Geospatial Information Authority of Japan, Kitasato 1, Tsukuba 305-0811, Japan
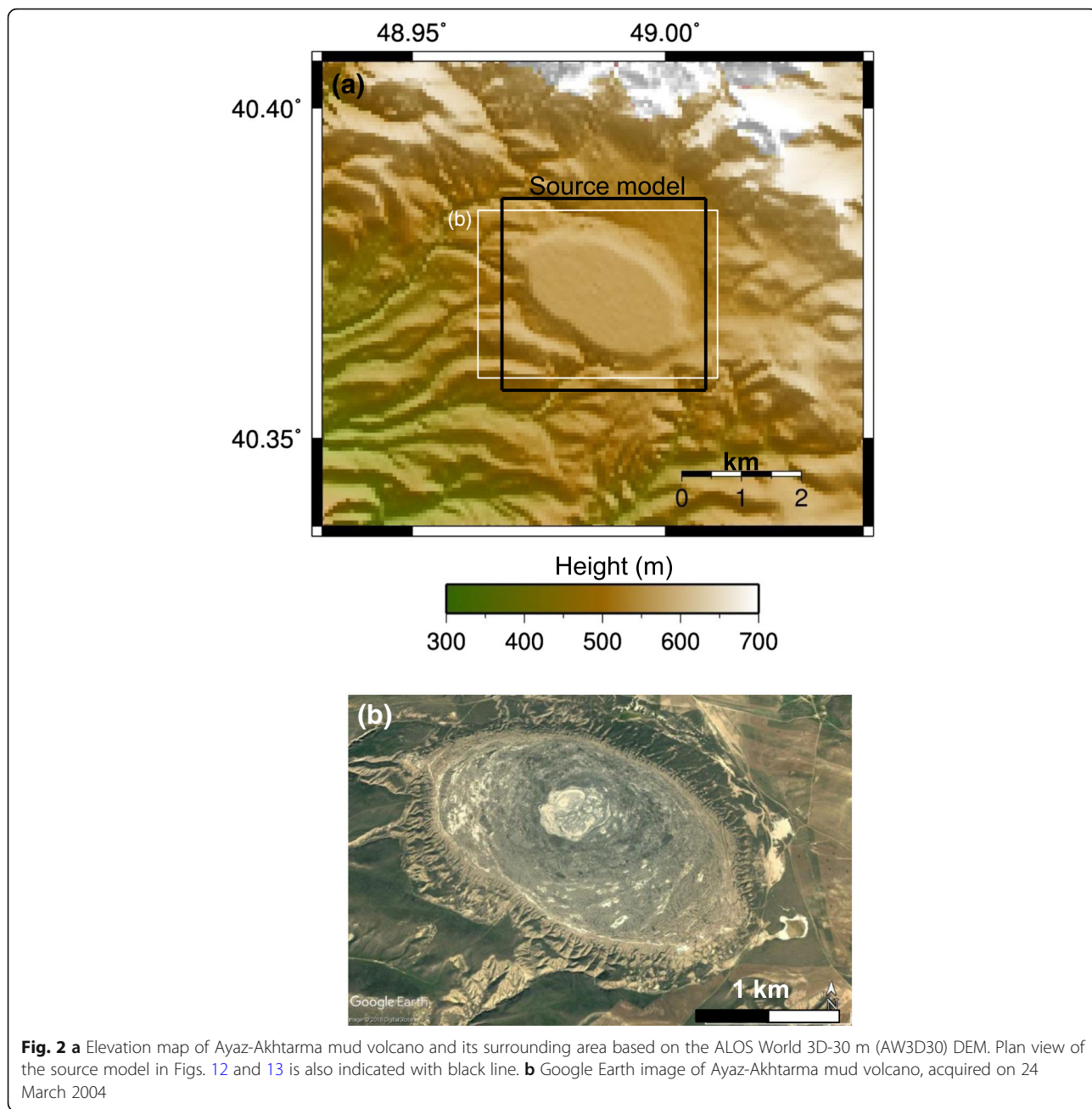Full list of author information is available at the end of the article

generated not only from the compaction of initially retained water by the overburden layer but also from the biogenic gas produced at depth from organic matter (Dimitrov, 2002). Compressive tectonic stress also contributes to higher pore-fluid pressures. The higher content of water and gas will significantly reduce the bulk density, shear modulus, and viscosity, allowing the layer to flow. However, the actual subsurface geometry and locations of such fluid-rich muddy masses remain uncertain.

Using satellite-based synthetic aperture radar (SAR), we can image ground surfaces with a resolution on the order of ten meters or less, regardless of weather and sunlight. Taking the difference of the phase values of SAR images at different times, the interferometric SAR (InSAR) technique allows us to map surface displacements with unprecedented spatial resolution, with an accuracy of a few centimeters, and has been used to study earthquake faults and volcanic magma sources (e.g., Massonnet and Feigl, 1998; Bürgmann et al., 2000; Hanssen, 2001; Simons and Rosen, 2015). While there have been numerous applications of InSAR to surface

deformation mapping at magmatic volcanoes, there are relatively few studies on its application to mud volcanoes, with the exception of the Lusi mud volcano eruption in Indonesia (e.g., Fukushima et al., 2009; Aoki and Sidiq, 2014).

Azerbaijan is located near the eastern edge of the Greater Caucasus and the western edge of the Caspian Sea and is one of the countries with the highest national populations of mud volcanoes (Fig. 1). Mud volcanoes in Azerbaijan are mostly located along the anticlinal structures found throughout the country (e.g., Bonini, 2012). While there have been a couple of pioneering studies that applied InSAR technique to detect the displacements due to mud volcanoes in Azerbaijan in the early 2000s (Hommels et al., 2003; Mellors et al., 2005), Antonielli et al. (2014) was the first to unequivocally reveal the surface displacements at four mud volcanoes in Azerbaijan with the uses of C-band Envisat/ASAR images gathered from 2003 to 2005. In particular, the study of the Ayaz-Akhtarma mud volcano (Fig. 2) revealed significant radar line-of-sight (LOS) changes, which were negative and positive in the eastern half and western half of the site, respectively. As the

Fig. 1 Location of Ayaz-Akhtarma mud volcano, indicated with red triangle. Orange, red, and blue rectangles represent the imaging areas covered by ALOS/PALSAR ascending, ALOS-2/PALSAR-2 ascending, and ALOS-2/PALSAR-2 descending tracks, respectively. Upper-left panel indicates the location of Azerbaijan and Caspian Sea

Fig. 2 a Elevation map of Ayaz-Akhtarma mud volcano and its surrounding area based on the ALOS World 3D-30 m (AW3D30) DEM. Plan view of the source model in Figs. 12 and 13 is also indicated with black line. **b** Google Earth image of Ayaz-Akhtarma mud volcano, acquired on 24 March 2004

negative and positive LOS changes indicate displacement toward and away from the satellite sensor, respectively, Antonielli et al. (2014) interpreted that these changes correspond to uplift and subsidence, respectively. However, the Envisat/ASAR images used in Antonielli et al. (2014) were acquired only from the descending track, with a fixed incidence angle. Because the radar LOS change derived by InSAR is a projection of the three-dimensional (3D) surface displacements onto the radar LOS direction, the observed LOS changes do not tell us the actual 3D displacement field, and the LOS is most sensitive to the vertical component of displacement because of its smaller incidence angle of ∼ 20–40 degrees. The interpretations of the derived LOS changes by Antonielli et al. (2014) thus remain inconclusive.

Here, we also apply InSAR technique to detect the surface displacements at the Ayaz-Akhtarma mud volcano, but use L-band (wavelength 23.6 cm) images from Advanced Land Observing Satellite (ALOS)/

Phased Array type L-band Synthetic Aperture Radar (PAL-SAR) and its successor, ALOS-2/PALSAR-2, collected from 2006 to 2010 and 2014 to 2017, respectively. The L-band SAR is known to be more advantageous than shorter wavelength microwave bands in terms of interferometric coherence (Rosen et al., 1996), and hence allows improved unwrapping of the InSAR phase data. Moreover, we process the SAR images acquired from both ascending and descending tracks, which will help to judge if vertical displacements dominate over horizontal displacements. We also apply a multiple-aperture interferometry (MAI) technique to derive the surface displacements that are parallel to the satellite flight direction in order to complement the InSAR data (Bechor and Zebker, 2006), since InSAR phase is insensitive to these along-track (near north-south) displacements. We can thus infer the full 3D displacements at the Ayaz-Akhtarma mud volcano. Based on these displacements' data and analytical solutions of elastic dislocation theory in an elastic half-space, we derive a source model that consists of a convex fault surface with normal faulting and strike-slip, which we will use to investigate the on-going processes and their relation to the stress regime.

Methods/Experimental

Figure 1 shows the areas covered by ALOS/PALSAR for its ascending path and by ALOS-2/PALSAR-2 for both its ascending and descending paths; note that the look direction from the ascending tracks is opposite to that used by Antonielli et al. (2014). Details on the ALOS/ALOS-2 data used are listed in Tables 1, 2, 3, and 4. SAR data was processed using GAMMA software (Wegmüller and Werner, 1997). To acquire interferograms with high coherence, we formed interferometric pairs, making each temporal separation as shorter as possible. We analyzed these data such that the slave data become the next master data, and so on. We used the ALOS World 3D-30 m (AW3D30) digital elevation model (DEM) and the precision orbit data to eliminate topographic and orbital fringes, respectively. Since the interferograms still included long-wavelength phase trends, we removed these by fitting low-order polynomials (in view of the derived spatial scale of ground deformation, we feel that this removal does not affect the detection of the deformation signals). For the step of phase unwrapping, we used the minimum cost flow algorithm (Costantini, 1998).

The basic algorithm of MAI is described in Barbot et al. (2008). In the MAI method, we split the total aperture time into forward-looking and backward-looking times and from these generate two single-look complex images. We then create forward and backward interferograms whose LOS directions are different. Taking the difference between the forward and backward interferograms, MAI provides us with the displacements projected along the satellite flight direction. Although

Table 1 ALOS/PALSAR datasets for interferograms in Fig. 3. All data sets are acquired from the ascending track (mostly from the south to the north) with an incidence angle 38.7° at the image center and a heading angle of − 10.1° measured clockwise from the north. The path and frame of all pairs are 573 and 800, respectively. Bperp means a perpendicular baseline

Pair no.	Date (yyyy/mm/dd)	Bperp (m)	Temporal baseline (days)
P1	2006/12/28–2007/02/12	1439	46
P2	2007/02/12–2007/06/30	614	138
P3	2007/06/30–2007/08/15	291	46
P4	2007/08/15–2007/09/30	271	46
P5	2007/09/30–2007/12/31	346	92
P6	2007/12/31–2008/04/01	1287	92
P7	2008/04/01–2008/05/17	199	46
P8	2008/05/17–2008/07/02	− 3292	46
P9	2008/07/02–2008/08/17	− 2829	46
P10	2008/08/17–2008/10/02	1015	46
P11	2008/10/02–2008/11/17	427	46
P12	2008/11/17–2009/01/02	181	46
P13	2009/01/02–2009/02/17	569	46
P14	2009/02/17–2009/08/20	754	184
P15	2009/08/20–2009/10/05	501	46
P16	2009/10/05–2010/01/05	488	92
P17	2010/01/05–2010/02/20	693	46
P18	2010/02/20–2010/04/07	152	46
P19	2010/04/07–2010/05/23	73	46
P20	2010/05/23–2010/07/08	52	46
P21	2010/07/08–2010/08/23	378	46
P22	2010/08/23–2011/01/08	880	138
P23	2011/01/08–2011/02/23	696	46

the measurement precision is lower than that of InSAR, with a precision on the order of about 10 cm (Bechor and Zebker 2006; Barbot et al. 2008; Jung et al. 2009), the MAI data complements that obtained by InSAR and allows us to derive 3D displacements through the combination of both techniques. In the MAI processing, the multi-look size was set 2 and 4 in range and azimuth directions, respectively, and we also applied Goldstein-Werner's adaptive spectral filter with the exponent of 0.7 to smooth the signals (Goldstein and Werner 1998).

Results
Observation results

In Figs. 3 and 4, we show the observed ALOS and ALOS-2 InSAR data, both derived from the ascending path; details are shown in Table 1 for P1–P23 and

Table 2 ALOS-2/PALSAR-2 data sets for interferograms in Fig. 4. The A and D stand for ascending and descending (mostly from the north to the south) orbits. The path and frame of the ascending and descending datasets are 176–800 and 71–2800, respectively. The incidence angle of the ascending and descending datasets are 31.4° and 36.3°, respectively. Heading angles of ascending and descending datasets are − 10.8 and − 169.8°, respectively

Pair no.	Orbit	Date (yyyy/mm/dd)	Bperp (m)	Temporal baseline (days)
P24	A	2014/09/17–2014/11/26	− 16	70
P25	A	2014/11/26–2015/02/04	98	70
P26	A	2015/02/04–2015/04/29	49	84
P27	A	2015/04/29–2015/07/08	90	70
P28	A	2015/07/08–2015/09/16	− 125	70
P29	A	2015/09/16–2016/06/08	31	266
P30	A	2016/06/08–2016/09/14	− 88	98
P31	A	2016/09/14–2016/11/23	43	70
P32	A	2016/11/23–2017/07/05	− 104	224
P33	D	2016/03/23–2016/06/01	− 360	70
P34	D	2016/06/01–2017/03/22	490	294
P35	D	2017/03/22–2017/05/31	− 439	70

Table 2 for P24–P32. Although they show diverse patterns of LOS changes, which we will discuss later in this paper, all of the results indicate that the western and eastern sectors across a N-S trending boundary near the center of the mud volcano show the signals in opposite sign. Figure 3 indicates that the surface approached the satellite in the west sector and moved away from the satellite in the east sector, respectively. The 23 interferograms in Fig. 3 are stacked to represent cumulative LOS changes in Fig. 5a. The cumulative LOS displacements of the western and the eastern sectors are around − 2.5 m and + 3.5 m, respectively, during the period of December 28, 2006, to February 23, 2011. In Fig. 4, for the ALOS-2 data, we can see essentially the same

Table 3 ALOS/PALSAR datasets for MAI images in Fig. 6. Details of the orbit, incidence, and heading angle are the same as in Table 1

Pair no.	Date (yyyy/mm/dd)	Bperp (m)	Temporal baseline (days)
P36	2006/12/28–2007/06/30	2054	184
P37	2007/06/30–2007/12/31	908	184
P38	2007/12/31–2008/07/02	− 1813	184
P39	2008/07/02–2009/02/17	− 646	230
P40	2009/02/17–2009/08/20	754	184
P41	2009/08/20–2010/01/05	990	138
P42	2010/01/05–2010/08/23	1347	230
P43	2010/08/23–2011/02/23	1575	184

Table 4 ALOS-2/PALSAR-2 data sets for MAI images in Fig. 7. Details of the orbit, incidence, and heading angle are the same as in Table 2

Pair no.	Orbit	Date (yyyy/mm/dd)	Bperp (m)	Temporal baseline (days)
P44	A	2014/09/17–2015/02/04	83	140
P45	A	2015/02/04–2015/09/16	− 85	224
P46	A	2015/09/16–2016/06/08	31	266
P47	A	2016/06/08–2016/11/23	− 46	168
P48	A	2016/11/23–2017/07/05	− 104	224
P49	D	2016/03/23–2017/03/22	130	364

pattern of LOS changes as in the ALOS InSAR data. The cumulative interferogram for the data in Fig. 4 is shown in Fig. 5b, with minimum and maximum values of − 1.5 m and + 1.5 m for the western and eastern sectors, respectively, during the period of September 17, 2014, to July 5, 2017. Although there are only three interferometric pairs, the observed ALOS-2 InSAR data along the descending track (P33–P35 in Table 2) are shown in Fig. 4. Descending interferograms indicate that the spatial pattern of LOS changes is consistent with the previous study (Antonielli et al. 2014), which, as for the ascending track, show eastern and western sectors separated at the center of the mud volcano by a near N-S boundary (Figs. 3 and 4). The cumulative LOS changes based on the three interferograms are shown in Fig. 5c, up to + 25 cm and − 50 cm for the western and eastern sectors, respectively, during the period of March 23, 2016, to May 31, 2017.

The LOS changes in ascending and descending orbits indicate that the areas near and far from the satellite show negative and positive changes, respectively. This, in turn, suggests that the nearside areas are approaching the satellite and the farside areas are moving away from the satellite. Hence, we can conclude that the LOS changes are mostly dominated by horizontal, rather than vertical, displacements. Because InSAR LOS change is most sensitive to the vertical component, we may observe similar spatial patterns in the LOS changes with the same signs, regardless of ascending and descending orbits, when the surface displacements are dominated by subsidence or uplift signals over flat areas (e.g., Aoki and Sidiq 2014). Our observations, however, clearly demonstrate that the observed LOS changes are not entirely due to the vertical displacements and that it is critically important to view one area from various directions.

In Fig. 6, we show the LOS change time series for ALOS (Fig. 6a) and ALOS-2 (Fig. 6b) data along the ascending orbit, which were derived by averaging the LOS change data in the western and eastern areas marked in Fig. 6c. These results indicate that the LOS changes are largely linear with some temporal fluctuations. The
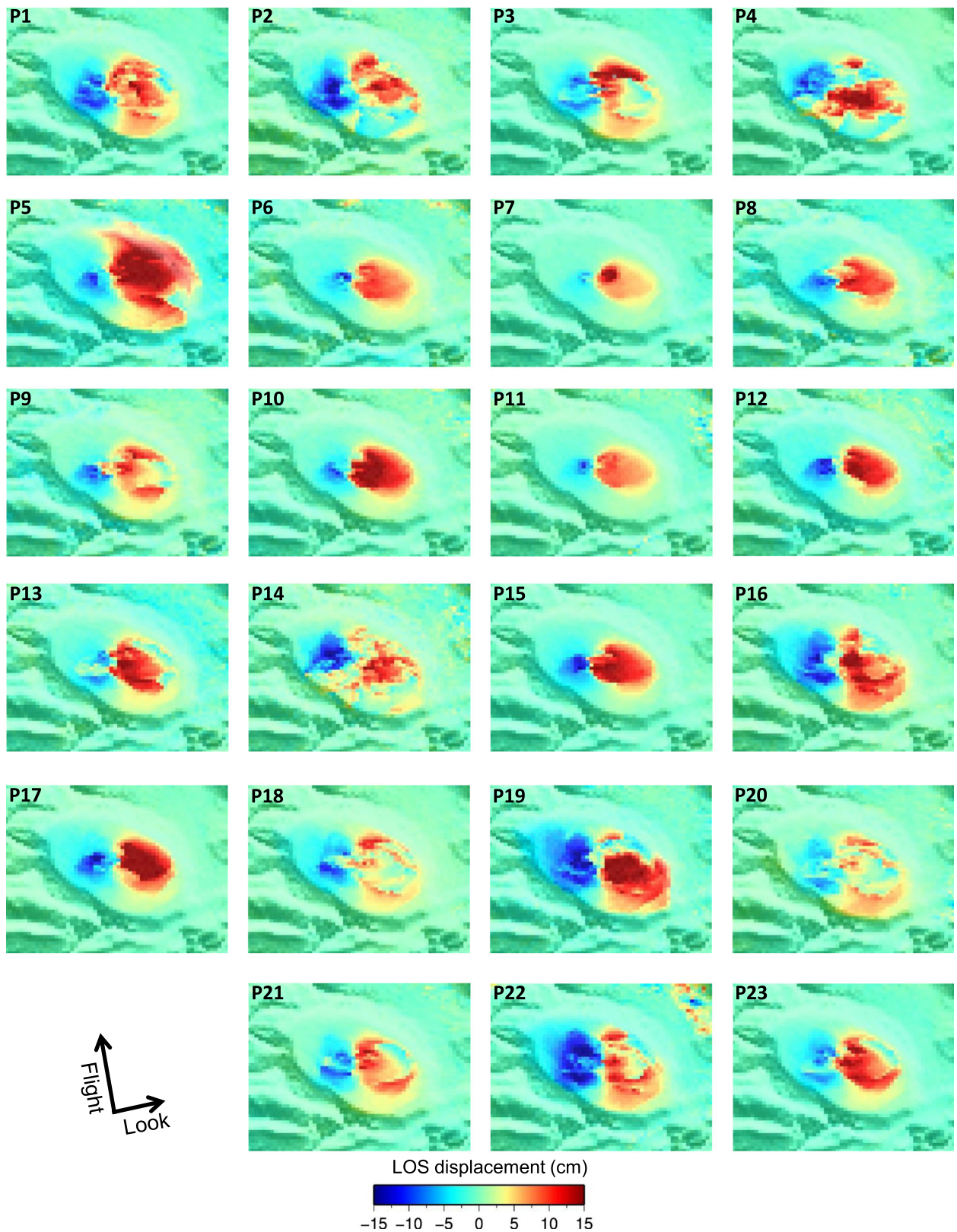
Fig. 3 Observed unwrapped InSAR images derived from ALOS/PALSAR ascending track data (path 573, frame 800). Positive and negative signals indicate the LOS changes away from and toward the satellite, respectively. Details of each data set are described in Table 1. Two arrows at the lower left indicate the satellite flight direction and beam radiation direction
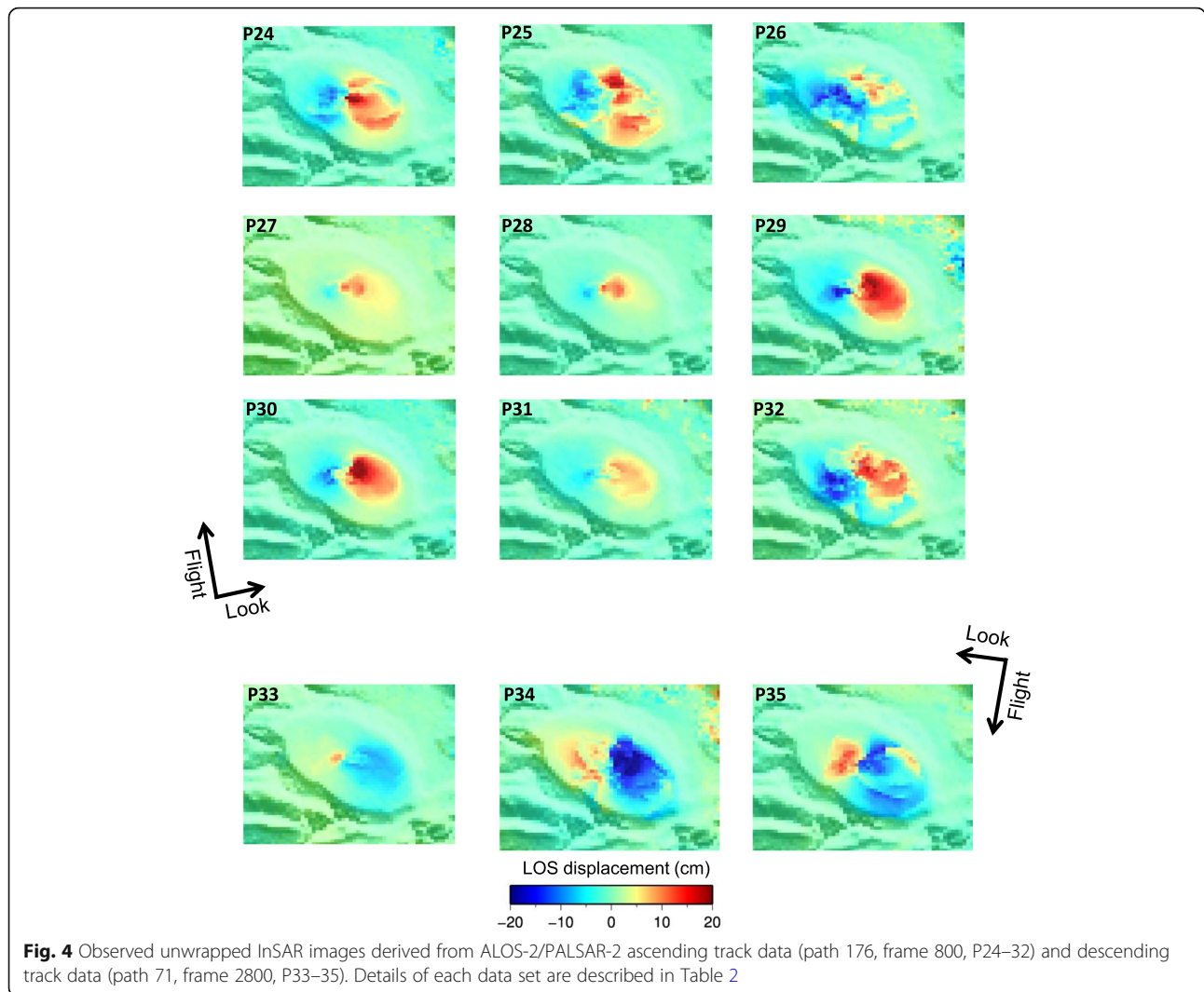
Fig. 4 Observed unwrapped InSAR images derived from ALOS-2/PALSAR-2 ascending track data (path 176, frame 800, P24–32) and descending track data (path 71, frame 2800, P33–35). Details of each data set are described in Table 2

inferred LOS velocities of the western and eastern parts of the ALOS data are − 31 cm/year and + 54 cm/year, and those of the ALOS-2 data are − 19 cm/year and + 35 cm/year, respectively. The larger velocities of the ALOS data compared to that of the ALOS-2 data are presumably due to the differences in the unit vectors of LOS directions, which are $(e_e, e_n, e_z) = (0.6157, 0.1085, -0.7804)$ for ascending ALOS and $(e_e, e_n, e_z) = (0.5120, 0.0974, -0.8535)$ for ascending ALOS-2. This indicates that the LOS vector of ALOS is more sensitive to horizontal displacement than that of the ALOS-2 data.

As noticed from the e_n component of the LOS vectors above, InSAR LOS changes are most insensitive to the north-south displacement because of the satellites near-polar orbit. To reveal the north-south displacement and thus to elucidate the 3D displacements, we employ MAI approach. The observed ALOS MAI data along the ascending path (Table 3) are shown in Fig. 7; the P38 data is much noisier due to lower coherence. The

positive and negative signals indicate the displacements projected along and opposite to the satellite flight direction, respectively. The observed MAI displacements show that the southern part of the mud volcano is represented by significant large negative signals, indicating that the southern portion moved opposite to the satellite flight direction. In Fig. 8, we present the observed MAI using ALOS-2 data along the ascending track (P44–P48 in Table 4). As shown in the ALOS MAI data, we can observe a similar pattern of displacements in the southern sector. Moreover, we can identify the displacements along the satellite flight direction, which were not clearly detected by the ALOS data in the northern sector. In Fig. 9a, we show the cumulative along track displacements of the eight ALOS MAI data, which reached up to − 7 m in the southern sector during the same period as the ALOS InSAR data. The stacked image of the five ALOS-2 MAI data is shown in Fig. 9b and indicates that the displacements of the northern and southern sectors
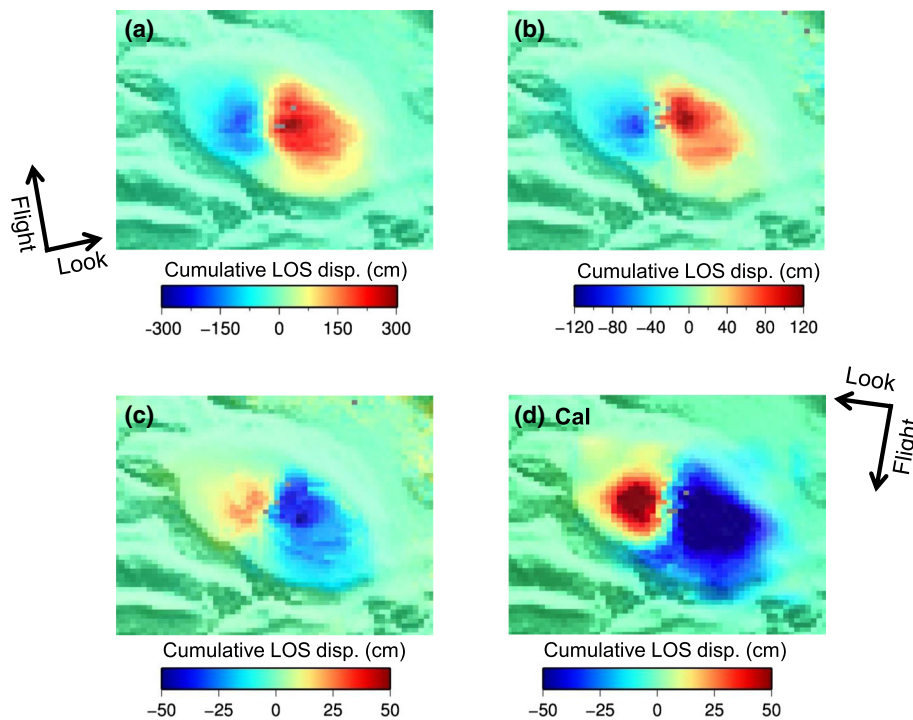
Fig. 5 Cumulative observed LOS changes derived from **a** ALOS/PALSAR data (P1-23), **b** ALOS-2/PALSAR-2 ascending data (P24–32), and **c** ALOS-2/PALSAR-2 descending data (P33–35). **d** Calculated ALOS-2/PALSAR-2 descending data, based on the slip distribution model in Fig. 12
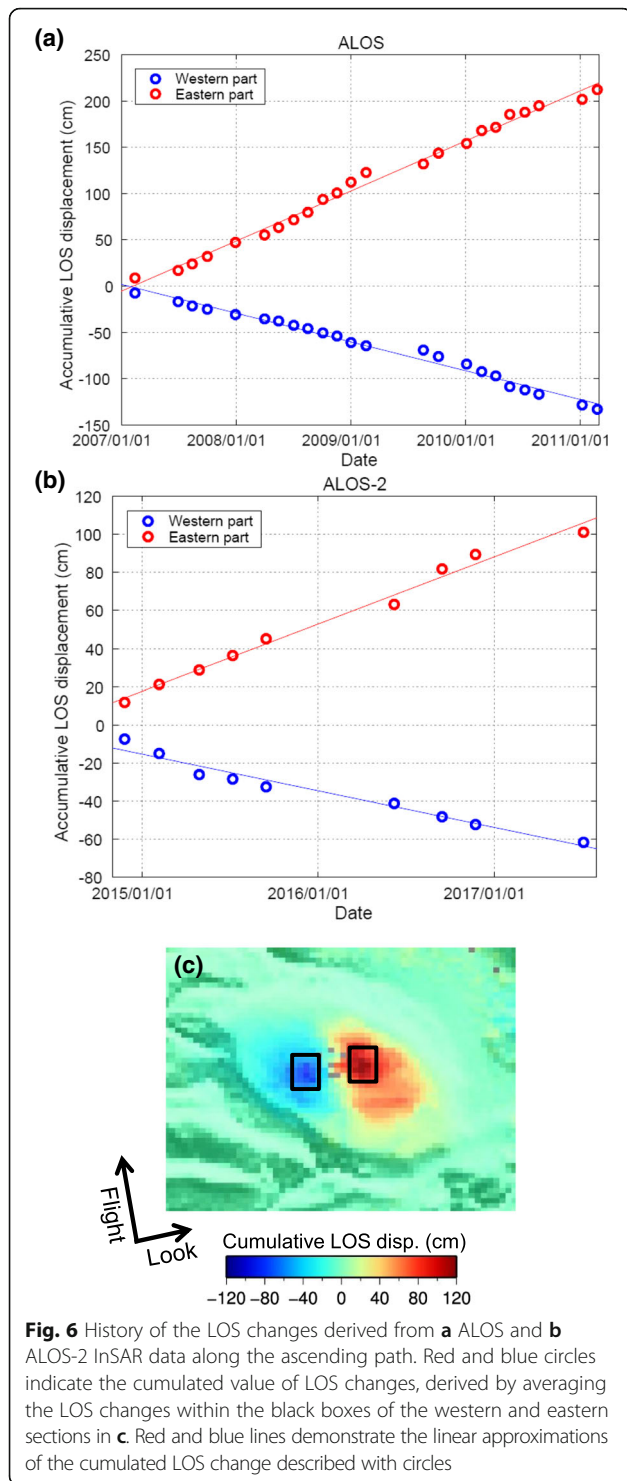
reached up to + 1.5 m and − 4.0 m along the flight direction, respectively. The observed MAI data along the descending path (P49 in Table 4) is also shown at the bottom of Fig. 8; we show this pair because it covers a longer temporal period with shorter perpendicular baseline. Although there is only one descending MAI dataset, *which* is still a bit noisy, the overall spatial pattern is consistent with that detected in the ascending MAI data, namely, large positive and small negative signals, which are separated around the middle of the mud volcano, with a near east-west boundary.

We estimate the 3D surface displacements, using InSAR and MAI measurements acquired from both ascending and descending paths. Because the observation period is different for the ascending and descending datasets, and the surface displacements appear to have been constantly taking place in view of the present and previous observation results (Antonielli et al. 2014), we converted the cumulative LOS and MAI changes (Figs. 5b, c, 9b, and 8 (P49)) into average velocities for simplicity. The calculation method to map the 3D displacements from the observation data is basically the same as those used in several previous studies (e.g., Wright et al. 2004; Jung et al. 2011). The inferred 3D displacements are shown in Fig. 10, which consists of (a) north-south, (b) east-west, and (c) up-down displacements; we should note that each color scale in Fig. 10 is different. They indicate very large north-south horizontal

displacements and smaller vertical displacements. We should note that the largest north-south displacements could only be inferred by using the MAI technique. In Fig. 10a, the broad area of the southern sector shows southward motion at a rate of ∼ 1 m/year. In Fig. 10b, the east-west component indicates extension by up to 80 cm/year in both easterly and westerly directions in the eastern and western sectors, respectively. Considering all the components, the results indicate that this mud volcano has been extending horizontally from the center, with southward displacements being most significant, and with some minor subsidence and possible uplift in places. The data scatter outside the mud volcano suggests the errors by as much as 10 cm/year.

Source modeling

To account for and interpret the observed cumulative InSAR and MAI data, we develop a fault source model, based on the dislocation theory in an elastic half-space. Although the analytical solutions by Okada (1985) have been widely used to explain surface displacements, they are derived on the assumption of rectangular dislocation elements and thus will generate mechanically incompatible gaps or overlaps in the case of a non-planar fault plane. Whereas the analytical solutions for rectangular dislocation elements are useful, those due to triangular dislocation elements are more versatile and allow us to represent more complex fault geometries (Maerten et al.

Fig. 6 History of the LOS changes derived from **a** ALOS and **b** ALOS-2 InSAR data along the ascending path. Red and blue circles indicate the cumulated value of LOS changes, derived by averaging the LOS changes within the black boxes of the western and eastern sections in **c**. Red and blue lines demonstrate the linear approximations of the cumulated LOS change described with circles

2005; Furuya and Yasuda 2011). We construct triangular meshes for the non-planar planes using Gmsh software (Geuzaine and Remacle 2009). The size of each side of the triangular mesh is approximately 150 m. To calculate Green's function of surface displacements

due to triangular dislocation elements, we use the MATLAB code produced by Meade (2007), assuming a Poisson ratio of 0.3.

In order to derive physically plausible distributions, we use a non-negative least squares method that constrains the slip directions (e.g., Simons et al. 2002), whereas we allow distinct strike-slip directions, depending on the dipping direction of each segment as noted below. We also apply a constraint on the smoothness of the slip distributions, using an umbrella operator (Maerten et al. 2005; Furuya and Yasuda 2011). We use the cumulative displacements acquired from the ascending orbit in the inversion (Fig. 11a–d). We do not invert for the descending orbit data because of the lack of cumulative displacement data for this orbit compared to the ascending orbit. Instead, based on the derived source model, we can compute descending and 3D data, with which we will compare the observed ones so that we can check the consistency of source modeling.

The location and geometry of the source fault are the most important factors in reducing the misfit residuals and were derived by trial-and-error (e.g., Furuya and Yasuda 2011; Abe et al. 2013; Himematsu and Furuya 2015). To reproduce the large horizontal and minor vertical displacements, we set a convex source surface to be dipping most significantly toward the south with minor dip toward east, west, and north; the shallowest point of the convex surface is located beneath the center of the mud volcano. Thereby, we allow for radially distributed normal fault slip on the convex surface. To express oblique normal faulting, we imposed right lateral and left lateral strike-slip on the west-dipping and east-dipping segment, respectively; no such constraint was imposed on the north-south trending normal fault slip for simplicity. To generate the triangular meshes with Gmsh, we initially assigned the 3D coordinates at the 8 control points along the border of the surface. The plane and 3D views are shown in Figs. 2a, 12, and 13, respectively; it should be noted that the scales for the vertical and horizontal axes are different, and the slope of the source plane is exaggerated in Figs. 12 and 13. Although the source surface is convex, the height differences are at most 50 m over the entire surface extending ~ 3 km. Nonetheless, we consider that the curvature is important because the observed large southward horizontal displacements and minor subsidence are most significantly explained by the large southward normal fault slip.

In Figs. 12 and 13, we show the optimum fault slip amplitude distribution and slip vectors on each segment, assuming that the slip occurs at a constant rate; Figs. 12 and 13 are derived from the ascending path data from ALOS and ALOS-2, respectively. The shallowest point of the convex surface is located at a depth of 25 m. Normal dip slip is dominant on the southern part of the
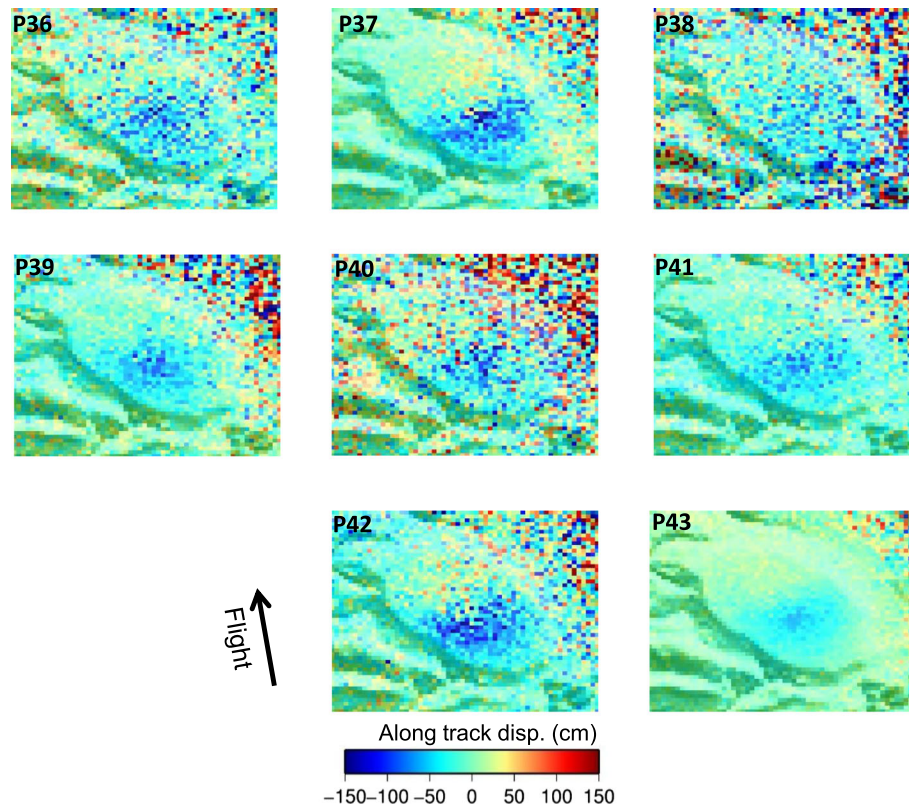
Fig. 7 Observed MAI data derived from ALOS/PALSAR ascending track data (path 573, frame 800). Positive and negative signals indicate the horizontal displacement projected in the direction of the satellite flight and the opposite direction, respectively. Details of each data set are described in Table 3

source plane and has maximum slip amplitudes around the depth of 35 m of up to 8 m (ALOS, Fig. 12c) and 4 m (ALOS-2, Fig. 13c). Moreover, we need to include "strike-slip" components on the western and eastern slope on the surface to represent the oblique normal dip slip. When we set the shallowest point further deeper by ~ 30 m, the estimated normal dip-slip amplitude was larger by ~ 1 m, whereas the misfit residuals became more significant.

Based on the estimated slip distributions, we compute the surface deformation projected onto the LOS and along the satellite track direction (Fig. 11e–h) and the misfit residuals (Fig. 11i–l). Although some residuals remain, the calculated surface displacements can largely reproduce the cumulative observations. Moreover, we show the computed 3D displacements (Fig. 10d–f) and descending InSAR data (Fig. 5d), both of which are based on the derived source model. Although we notice some differences particularly in the EW components (Fig. 10e), the calculated data turn out to largely reproduce the observed ones, which demonstrate the consistency of the source model. Although we tried setting a Mogi-type point source and a Yang-type spheroid

source, we could not explain the observed data with physically plausible volume changes. We also tested tensile opening and closure, but could not consistently explain the estimated 3D and descending data. We consider that our source model is probably the simplest in terms of its overall geometry and slip distribution within a framework of elastic dislocation theory, whereas we do not preclude more sophisticated models. We interpret the inferred source model in the following section and discuss the implications for mud volcanism.
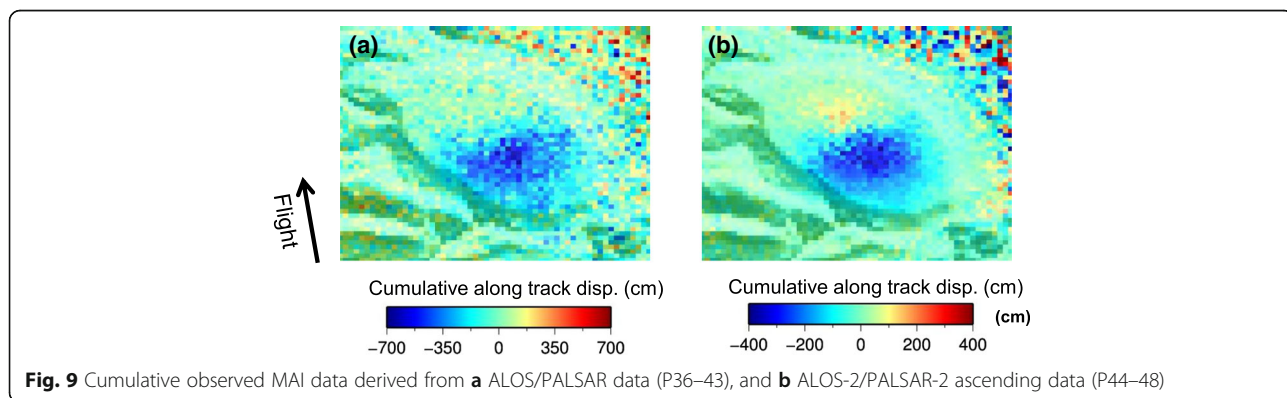
Discussion
Why are the LOS changes from ALOS1/2 data larger than those from Envisat data?
Comparing our observed interferograms with the results produced by Antonielli et al. (2014), we observe that the LOS changes in our study are much larger than those found in the previous study. The acquired cumulative LOS displacements of ALOS and ALOS-2 along the ascending track are up to 300 cm and 120 cm for about 4 and 2 years, respectively, and that of ALOS-2 along the descending track is up to 50 cm for about a year, whereas the cumulative LOS displacement calculated by

Fig. 8 Observed MAI data derived from ALOS-2/PALSAR-2 ascending track data (path 176, frame 800, P44–48) and descending track data (path 71, frame 2800, P49). Details of each data set are described in Table 4
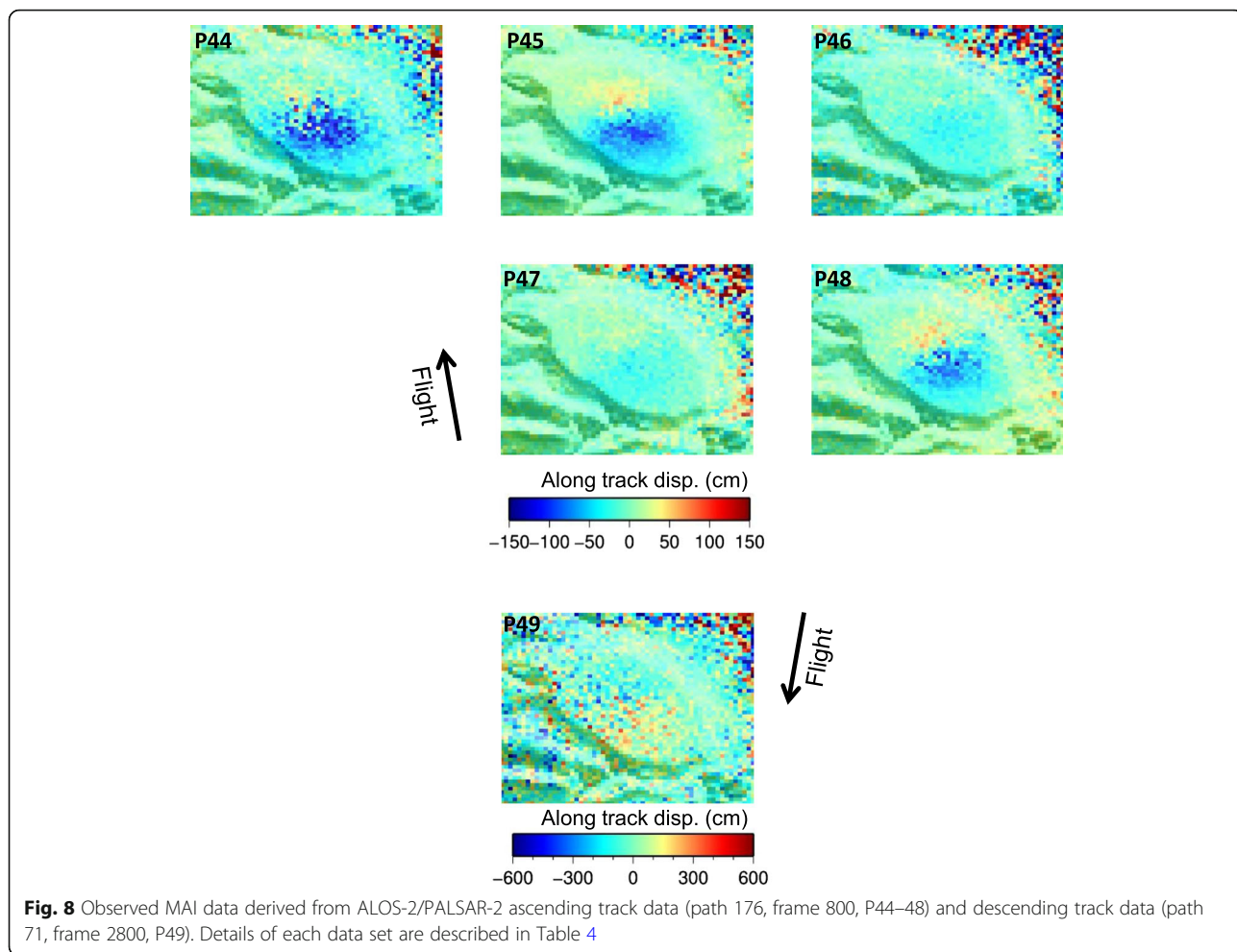
Antonielli et al. (2014) is up to 20 cm for about 2 years. This notable difference may be caused by two possible factors. One possibility is an increase in the activity of the mud volcano, and the other is a difference in the local incidence angle between the data sets. The incidence angles at the image center of the ascending ALOS, ascending ALOS-2, and descending ALOS-2 are 38.7°, 31.4°, and 36.3°, respectively, whereas the angle of the Envisat is 23°, while the local heading angle does not differ significantly between the data sets. With the heading angle of 10° counter-clockwise at mid-latitude, the unitary LOS vectors for Envisat/ASAR are (e_e, e_n, e_z) = (0.416, 0.073, − 0.906). Compared to the LOS vectors for ALOS1/2 noted earlier, Envisat/ASAR is apparently more sensitive to vertical and less sensitive to horizontal displacements. As the inferred 3D displacements show,
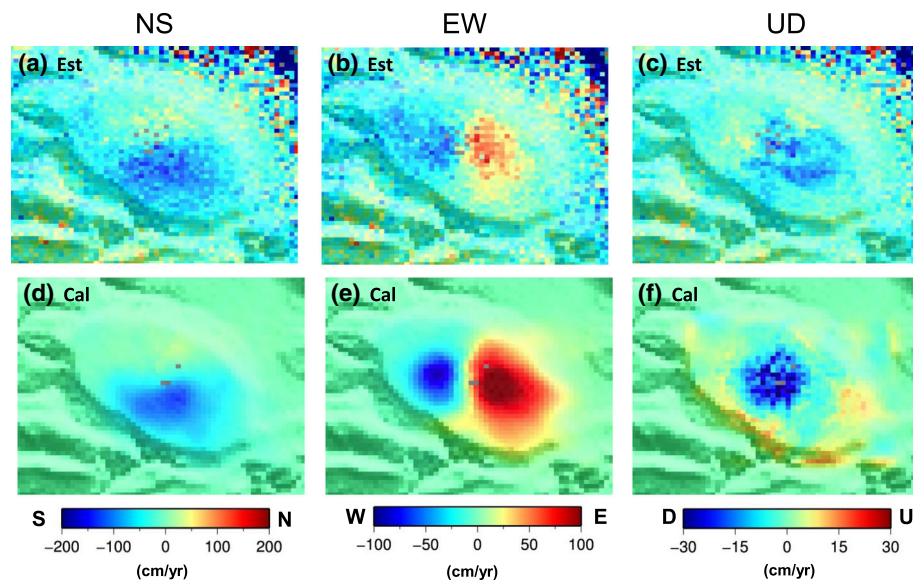

Fig. 9 Cumulative observed MAI data derived from **a** ALOS/PALSAR data (P36–43), and **b** ALOS-2/PALSAR-2 ascending data (P44–48)

Fig. 10 3D displacements derived from both InSAR and MAI data, assuming constant velocity. **a** North-south displacement. **b** East-west displacement. **c** Up-down displacement. Also shown in **d**, **e**, and **f** are the predicted 3D displacements from the slip distribution model in Fig. 12. Positive signals indicate northward, eastward, and uplift movement, for **a**, **d**; **b**, **e**; and **c**, **f** respectively. Note the difference in the color bar scales

the largest displacements are due to north-south displacement, and the vertical displacement was the least significant, which is a rare occurrence to our knowledge. Using the derived 3D displacements in Fig. 10, we computed the LOS changes for the Envisat beam geometry. Indeed, the LOS changes for the Envisat beam turned out to be smaller than those due to the ALOS beam. However, the differences were not as striking as noted above. Thus, we cannot reject the first possibility.

Interpretations of the source model and the mud volcanism at Ayaz-Akhtarma

Although we could explain the cumulative LOS changes and MAI data with the use of the dislocation theory in elastic half-space, the inferred depth of the fault source is much shallower than those for earthquakes and magmatic eruptions, and the magnitudes of the estimated slip are so large that they may cast doubt on the validity of the use of elastic theory. We recognize that the elastic theory would be invalid in a strict sense for modeling of the observed large displacements, but we consider that the elastic dislocation theory is a helpful tool that can tell us the approximate location and geometry of the mechanical source. Moreover, because we inverted for the cumulative displacements instead of the short-term displacements, the inferred slip amplitude should be regarded as cumulative amplitude as well and may not be unreasonably large. Indeed, in view of each interferogram in Figs. 3 and 4, we can observe more complicated and non-smooth signals on the surface, which are rather

localized and not clearly shown in the observed cumulative LOS changes; such localized signals in each interferogram cannot be reproduced in the calculated cumulative LOS (Fig. 5) and MAI (Fig. 9) data, either. We might be able to regard those small-scale signals in each interferogram as a surface expression of local elastic failure. We consider that the cumulative signals simply obscure those small-scale signals, which appear at each interferogram but do not persist over time.

The source model consists of a convex surface on which normal dip slips are semi-radially distributed from the top but most significantly on the south-dipping portion. Under such slip systems, it is reasonable to observe subsidence signals around the center of the mud volcano (Fig. 10c, f). Although the source model does not explicitly include any overpressure forcing elements, the convex geometry could be maintained by constant injection of mud and gas onto the slip surface. We consider that there would exist feeder channels or pipes from deeper mud diapirs (mud chambers) connected to the convex surface, which, however, do not exert sufficient stress to cause surface displacements. Meanwhile, the origin of the significant normal fault slip might seem to be puzzling, considering that the study area is under a compressive stress regime in terms of the global stress field. However, we should recall that, like many mud volcanoes in Azerbaijan, Ayaz-Akhtarma mud volcano is located along anticline axes formed by the regional compressive stress field. We interpret that the mud and gas have reached the anticlinal trap, where intruded
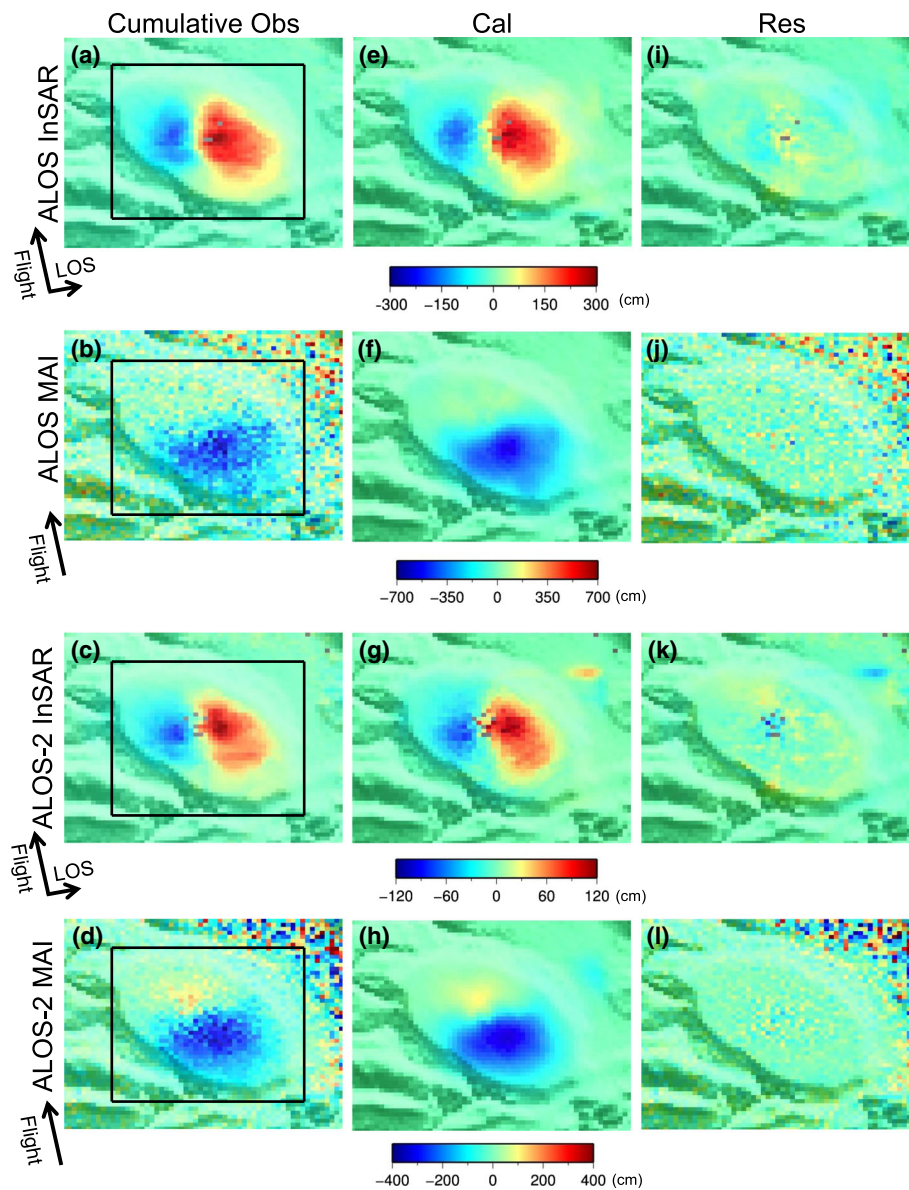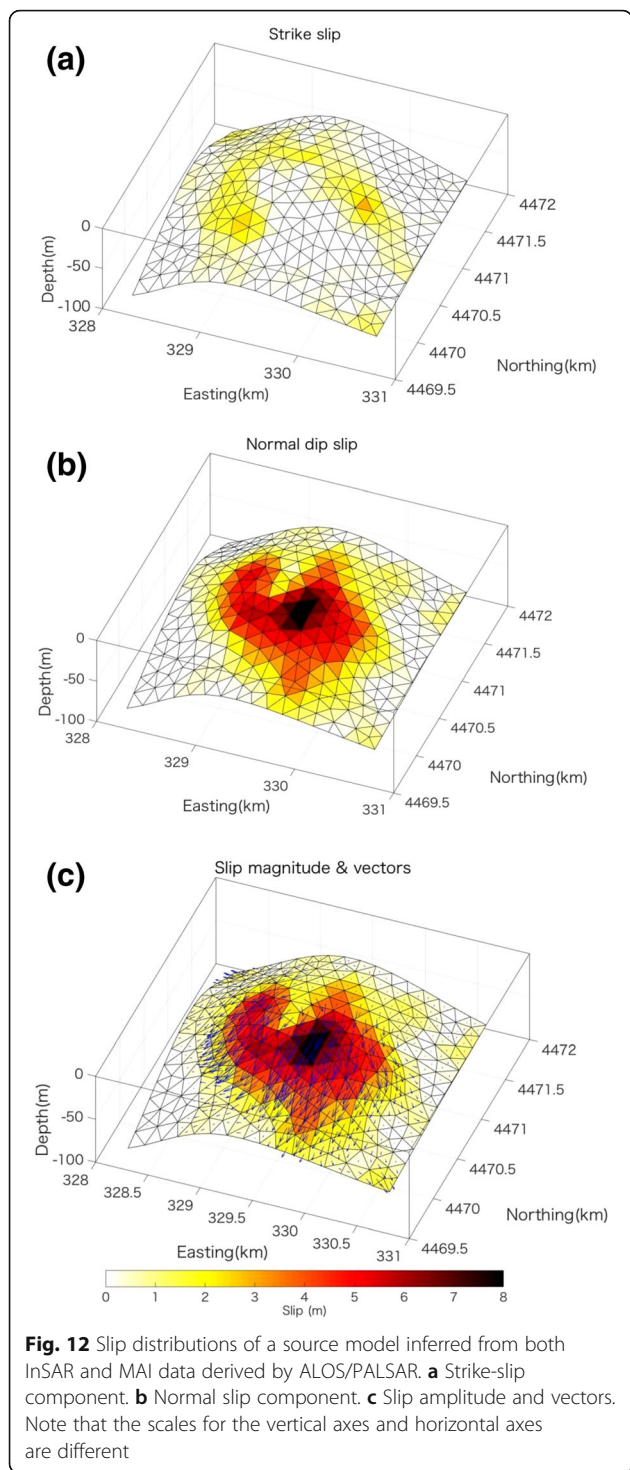
Fig. 11 Comparisons of cumulative observed data, calculated data, and the misfit residual. The left column (**a**–**d**) is the observed cumulative InSAR and MAI data, the middle one (**e**–**h**) is the calculated InSAR and MAI data derived from the source model in Figs. 12 and 13, and the right column (**i**–**l**) is the misfit between the observation and the calculation. The plan view of the source model in Figs. 11 and 12 is indicated with a black line

materials at very shallow depths are generating localized extensional stress and subsequent normal faulting.

Antonielli et al. (2014) performed a field survey and identified a 600 m-long fault or fracture, which we could also identify from a Google Earth image (Fig. 14b). Moreover, using Google Earth and USGS Landsat satellite images, we observed that the surface of the mud volcano is far from smooth, and such faults or fractures can be observed at many places on the surface (Fig. 14c). Our source model indicates that the largest normal fault

slip amplitude lies roughly in a north-south direction. The dominant reported by Antonielli et al. (2014) are mechanically consistent with our source model. Our source model could be used as a guide for further field survey at unexplored areas.

Despite the large slip inferred from the source modeling, there is no evidence for major eruptive episodes during the analyzed period. If there were significant eruptions, we could not generate unwrapped interferograms because surface failures and eruption deposits
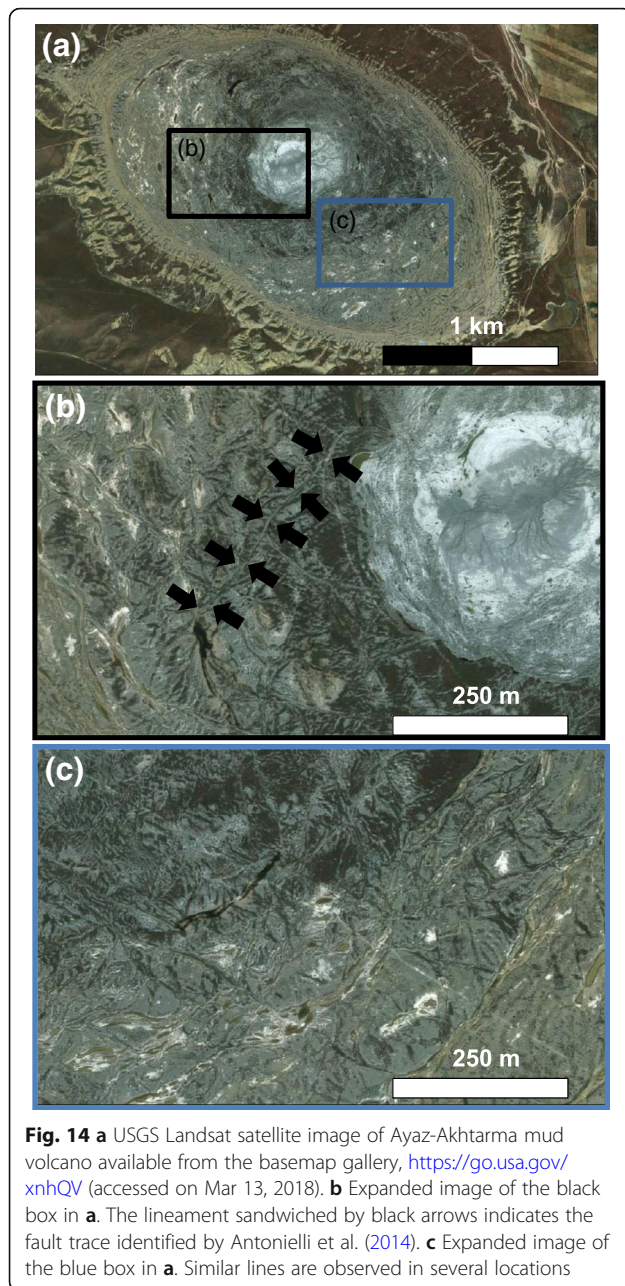
Fig. 12 Slip distributions of a source model inferred from both InSAR and MAI data derived by ALOS/PALSAR. **a** Strike-slip component. **b** Normal slip component. **c** Slip amplitude and vectors. Note that the scales for the vertical axes and horizontal axes are different

Fig. 13 Slip distributions of a source model inferred from both InSAR and MAI data derived by ALOS-2/PALSAR-2. **a** Strike-slip component. **b** Normal slip component. **c** Slip amplitude and vectors. Note that the scales for vertical axes and horizontal axes are different

from major mud eruptions would have caused the loss of interferometric coherence. However, small-scale eruptions and/or seepages of mud or gas seem to have been continuous (Dupuis et al., 2016). Those rather minor mud volcano activities presumably did not affect the present InSAR observations with a recurrence interval of
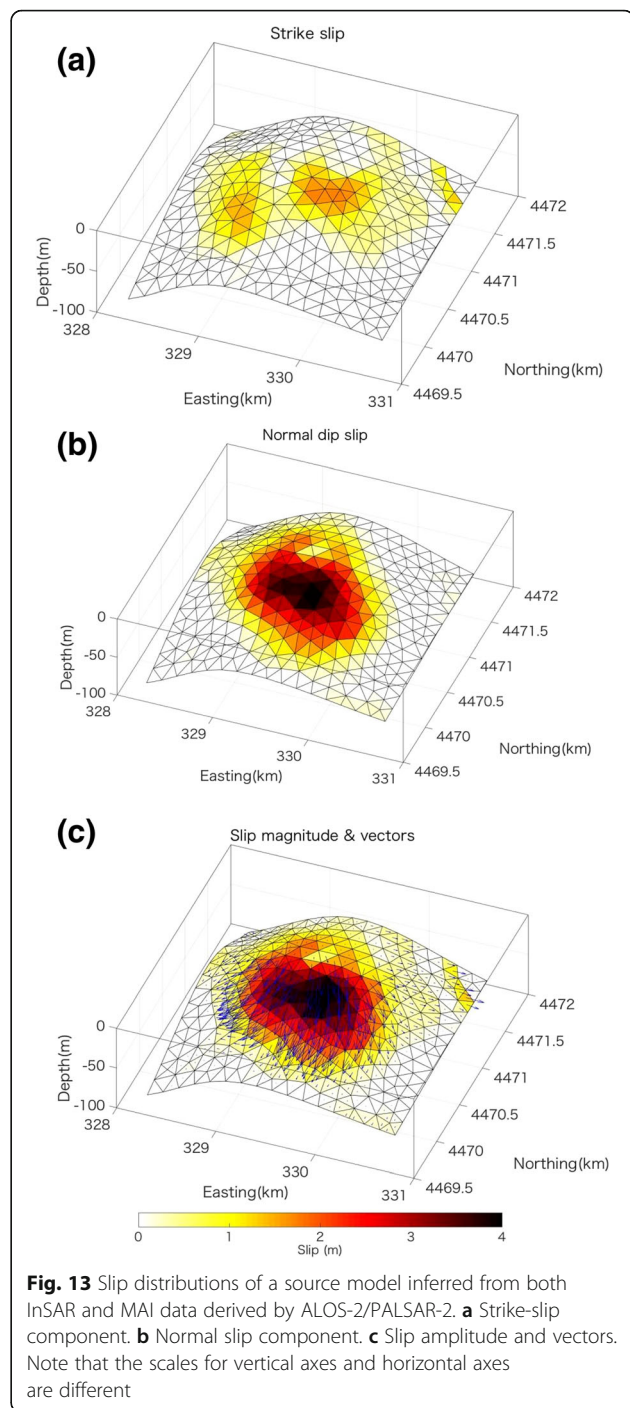
~ 50 days, whereas the large amplitude localized signals in Figs. 3 and 4 were probably due to minor eruptive episodes.

It is well known that the eruption of mud volcanoes is often triggered by earthquakes (e.g., Kopf 2002; Mellors et al. 2007; Manga et al. 2009 Bonini et al. 2016). Manga et al. (2009) proposed a relationship between an earthquake's magnitude and its hypocentral distance, which

Fig. 14 a USGS Landsat satellite image of Ayaz-Akhtarma mud volcano available from the basemap gallery, https://go.usa.gov/xnhQV (accessed on Mar 13, 2018). **b** Expanded image of the black box in **a**. The lineament sandwiched by black arrows indicates the fault trace identified by Antonielli et al. (2014). **c** Expanded image of the blue box in **a**. Similar lines are observed in several locations

predicts that a mud volcano eruption can be triggered by an earthquake with M5 or above occurring within a distance of 20 km. Unfortunately, we do not have any local observation data to correlate seismic events with the triggered eruption(s), but even if they did occur, any eruptions must have been minor episodes, as speculated above.

Conclusions

Using ALOS/PALSAR and ALOS-2/PALSAR-2 InSAR and MAI data, we detected the detailed surface displacements associated with the activity of Ayaz-Akhtarma

mud volcano. The MAI technique in particular turned out to be helpful in acquiring a more complete image of the surface deformation. By combining InSAR and MAI data, we were able to demonstrate that the actual displacements are dominated by horizontal, rather than vertical, components and that the north-south displacements are the largest. Our source model consists of semi-radially distributed normal dip-slip on a convex surface, on which mud and gas are continuously intruding.

Abbreviations
ALOS: Advanced Land Observing Satellite; InSAR: Interferometric synthetic aperture radar; LOS: Line of sight; MAI: Multiple-aperture interferometry; PALSAR: Phased Array type L-band Synthetic Aperture Radar; SAR: Synthetic aperture radar

Authors' contributions
KI processed and analyzed the ALOS-1/2 data. Both KI and MF have managed the research and drafted this manuscript. Both authors read and approved the final manuscript.

Competing interests
The authors declare that they have no competing interests.

Publisher's Note

Springer Nature remains neutral with regard to jurisdictional claims in published maps and institutional affiliations.

Author details
[1]Department of Natural History Sciences, Graduate School of Science, Hokkaido University, N10W8, Kita-ku, Sapporo 060-0810, Japan. [2]Department of Earth and Planetary Sciences, Faculty of Science, Hokkaido University, N10W8, Kita-ku, Sapporo 060-0810, Japan. [3]Geospatial Information Authority of Japan, Kitasato 1, Tsukuba 305-0811, Japan.

References
Abe T, Furuya M, Takada Y (2013) Nonplanar fault source modeling of the 2008 Iwate-Miyagi inland earthquake (Mw 6.9) in Northeast Japan. Bull Seismo Soc Am 103:507–518
Antonielli B, Monserrat O, Bonini M, Righini G, Sani F, Luzi G, Feyzullayev AA, Aliyev CS (2014) Pre-eruptive ground deformation of Azerbaijan mud volcanoes detected through satellite radar interferometry (DInSAR). Tectonophysics 637:163–177. https://doi.org/10.1016/j.tecto.2014.10.005

Aoki Y, Sidiq TP (2014) Ground deformation associated with the eruption of Lumpur Sidoarjo mud volcano, east Jana, Indonesia. J Volcanol Geotherm Res 278-279:96–102. https://doi.org/10.1016/j.jvolgeores.2014.04.012

Barbot S, Hamiel Y, Fialko Y (2008) Space geodetic investigation of the coseismic and postseismic deformation due to the 2003 M(w)7.2 Altai earthquake: implications for the local lithospheric rheology. J Geophys Res 113:B03403. https://doi.org/10.1029/2007JB005063

Bechor NBD, Zebker HA (2006) Measuring two-dimensional movements using a single InSAR pair. Geophys Res Lett 33:L16311. https://doi.org/10.1029/2006GL026883

Bonini M (2012) Mud volcanoes: indicators of stress orientation and tectonic controls. Earth Sci Rev 115:121–152. https://doi.org/10.1016/j.earscirev.2012.09.002

Bonini M, Rudolph ML, Manga M (2016) Long- and short-term triggering and modulation of mud volcano eruptions by earthquakes. Tectonophysics 672-673:190–211. https://doi.org/10.1016/j.tecto.2016.01.037

Bürgmann R, Rosen PA, Fielding EJ (2000) Synthetic aperture radar interferometry to measure Earth's surface topography and its deformation. Annu Rev Earth Planet Sci 28:169–209

Costantini M (1998) A novel phase unwrapping method based on network programming. IEEE Trans Geosci Remote Sens 36(3):813–821

Dimitrov LI (2002) Mud volcanoes—the most important pathway for degassing deeply buried sediments. Earth Sci Rev 59:49–76. https://doi.org/10.1016/S0012-8252(02)00069-7

Dupuis M, Odonne F, Imbert P, Abbasov O, Figarov T, Dofal A, Vendeville B (2016) The Ayaz-Akhtarma mud volcano: an actively growing mud pie in the foothills of the Greater Caucasus, Azerbaijan. Paper presented at the 13th International Conference on Gas in Marine Sediments, Tromsø, pp 19–22 Norway September 2016

Fukushima Y, Mori J, Hashimoto M, Kano Y (2009) Subsidence associated with the LUSI mud eruption, East Java, investigated by SAR interferometry. Mar Pet Geol 26:1740–1750. https://doi.org/10.1016/j.marpetgeo.2009.02.001

Furuya M, Yasuda T (2011) The 2008 Yutian normal faulting earthquake (Mw 7.1), NW Tibet: non-planar fault modeling and implications for the Karakax fault. Tectonophysics 511:125–133. https://doi.org/10.1016/j.tecto.2011.09.003

Geuzaine C, Remacle JF (2009) Gmsh: a 3-D finite element mesh generator with built-in pre- and post-processing facilities. Int J Numer Methods Eng 79: 1309–1331. https://doi.org/10.1002/nme.2579

Goldstein RM, Werner CL (1998) Radar interferogram filtering for geophysical application. Geophys Res Lett 25:4035–4038. https://doi.org/10.1029/1998GL900033

Hanssen R (2001) Radar interferometry: data interpretation and error analysis Kluwer academic publishers, p 328 Netherlands pp

Himematsu Y, Furuya M (2015) Aseismic strike-slip associated with the 2007 dike intrusion episode in Tanzania. Tectonophysics 656:52–60. https://doi.org/10.1016/j.tecto.2015.06.005

Hommels A, Scholte KH, Munoz-Sabater J, Hanssen RF, Van der Meer FD, Kroonenberg SB, Aliyeva E, Huseynov D, Guliev I (2003) Preliminary ASTER and InSAR imagery combination for mud volcano dynamics, Azerbaijan. International Geoscience and Remote Sensing Symposium 3:1573–1575. https://doi.org/10.1109/IGARSS.2003.1294179

Jung HS, Lu Z, Won JS, Poland MP, Miklius A (2011) Mapping three-dimensional surface deformation by combining multiple-aperture interferometry and conventional interferometry: application to the June 2007 eruption of Kilauea volcano, Hawaii. IEEE Geosci Remote Sens Lett 8(1):34–38

Jung HS, Won JS, Kim SW (2009) An improvement of the performance of Multiple-Aperture SAR Interferometry (MAI). IEEE Trans Geosci Remote Sens 47(8):2859–2869

Kopf AJ (2002) Significance of mud volcanism. Rev Geophys 40:1–52. https://doi.org/10.1029/2000RG000093

Maerten F, Resor P, Pollard D, Maerten L (2005) Inverting for slip on three-dimensional fault surfaces using angular dislocations. Bull Seismol Soc Am 95(5):1654–1665. https://doi.org/10.1785/0120030181

Manga M, Brumm M, Rudolph ML (2009) Earthquake triggering of mud volcanoes. Mar Pet Geol 26:1785–1798. https://doi.org/10.1016/j.marpetgeo.2009.01.019

Massonnet D, Feigl KL (1998) Radar interferometry and its application to changes in the Earth's surface. Rev Geophys 36:441–500. https://doi.org/10.1029/97RG03139

Mazzini A (2009) Mud volcanism: processes and implications. Mar Pet Geol 26: 1677–1688

Mazzini A, Etiope G (2017) Mud volcanism: an updated review. Earth Sci Rev 168: 81–112. https://doi.org/10.1016/j.earscirev.2017.03.001

Meade BJ (2007) Algorithms for the calculation of exact displacements, strain, and stresses for triangular dislocation elements in a uniform elastic half space. Comput Geosci 33:1064–1075. https://doi.org/10.1016/j.cageo.2006.12.003

Mellors R, Kilb D, Aliyev A, Gasanov A, Yetirmishli G (2007) Correlations between earthquakes and large mud volcano eruptions. J Geophys Res 112:B04304. https://doi.org/10.1029/2006JB004489

Mellors RJ, Bunyapanasarn T, Panahi B (2005) InSAR analysis of the Absheron peninsula and nearby areas, Azerbaijan. Geodynamics and Seismicity NATO Science Series 51:201–209

Milkov AV (2000) Worldwide distribution of submarine mud volcanoes and associated gas hydrates. Mar Geol 167:29–42. https://doi.org/10.1016/S0025-3227(00)00022-0

Okada Y (1985) Surface deformation due to shear and tensile faults in a half-space. Bull Seismo Soc Am 75:1135–1154

Rosen PA, Hensley S, Zebker HA, Webb FH, Fielding EJ (1996) Surface deformation and coherence measurements of Kilauea volcano, Hawaii, from SIR-C radar interferometry. J Geophys Res 101(E10):23109–23125. https://doi.org/10.1029/96JE01459

Simons M, Fialko Y, Rivera L (2002) Coseismic deformation from the 1999 M_w 7.1 Hector Mine, California, earthquake as inferred from InSAR and GPS observations. Bull Seism Soc Am 92:1390–1402

Simons M, Rosen PA (2015) Interferometric synthetic aperture radar geodesy, in Schubert G (editor-in-chief): treatise in geophysics, vol 3, 2nd edn. Elsevier, Oxford, pp 339–385

Wegmüller U, Werner CL (1997) Gamma SAR processor and interferometry software. Proc. of the 3rd ERS symposium, European Space Agency Special Publication, ESA SP-414:1686–1692

Wright TJ, Parsons BE, Lu Z (2004) Toward mapping surface deformation in three dimensions using InSAR. Gephys Res Lett 31:L01607. https://doi.org/10.1029/2003GL018827